JGR Space Physics

RESEARCH ARTICLE
10.1029/2023JA031950

Key Points:

- This is the first report of longitudinal development of cosmic radio noise absorption (CNA) for storm-time substorms using six ground riometers at subauroral latitudes
- CNA enhancements expanded eastward (5 cases), westward (1 cases), and anti-sunward (1 case)
- Spatio-temporal development of CNA at subauroral latitudes corresponds to high energy electron drift in the inner magnetosphere

Supporting Information:

Supporting Information may be found in the online version of this article.

Correspondence to:

K. Shiokawa,
shiokawa@nagoya-u.jp

Citation:

Kato, Y., Shiokawa, K., Tanaka, Y., Ozaki, M., Kadokura, A., Oyama, S.-i., et al. (2024). Longitudinal development of cosmic noise absorption based on multipoint observations at subauroral latitudes during storm-time substorms on 25–28 August 2018. *Journal of Geophysical Research: Space Physics*, *129*, e2023JA031950. https://doi.org/10.1029/2023JA031950

Received 29 JUL 2023
Accepted 7 DEC 2023

Author Contributions:

Conceptualization: Kazuo Shiokawa
Data curation: Kazuo Shiokawa, Yoshimasa Tanaka, Mitsunori Ozaki, Akira Kadokura, Shin-ichiro Oyama, Alexey Oinats, Martin Connors, Dmitry Baishev
Formal analysis: Yuto Kato
Funding acquisition: Kazuo Shiokawa, Akira Kadokura, Martin Connors, Dmitry Baishev
Investigation: Yuto Kato
Methodology: Kazuo Shiokawa, Yoshimasa Tanaka
Project Administration: Kazuo Shiokawa, Akira Kadokura, Martin Connors, Dmitry Baishev

Longitudinal Development of Cosmic Noise Absorption Based on Multipoint Observations at Subauroral Latitudes During Storm-Time Substorms on 25–28 August 2018

Yuto Kato[1], Kazuo Shiokawa[1], Yoshimasa Tanaka[2,3,4], Mitsunori Ozaki[5], Akira Kadokura[2,3,4], Shin-ichiro Oyama[1,4,6], Alexey Oinats[7], Martin Connors[8], and Dmitry Baishev[9]

[1]Institute for Space-Earth Environmental Research, Nagoya University, Nagoya, Japan, [2]Joint Support-Center for Data Science Research/Polar Environment Data Science Center, Tachikawa, Japan, [3]The Graduate University for Advanced Studies, Hayama, Japan, [4]National Institute of Polar Research, Tachikawa, Japan, [5]Kanazawa University, Kanazawa, Japan, [6]University of Oulu, Oulu, Finland, [7]Institute of Solar-Terrestrial Physics, Siberian Branch of the Russian Academy of Sciences, Irkutsk, Russia, [8]Athabasca University, Athabasca, AB, Canada, [9]Yu.G. Shafer Institute of Cosmophysical Research and Aeronomy, Siberian Branch of the Russian Academy of Sciences, Yakutsk, Russia

Abstract Enhancements in electron density in the D-region ionosphere attributed to the precipitation of high-energy electrons, have previously been inferred from increases in cosmic radio noise absorption (CNA) using ground-based riometers. However, there have been few studies of CNA observations at multi-point stations distributed in longitudes. Thus, the spatio-temporal development of the global distribution of CNA is not well understood. In this study, we investigated the longitudinal extent of CNA using simultaneous riometer observations at six stations at subauroral latitudes in Canada, Alaska, Russia, and Iceland. These stations are located encircling the earth at ~60° north magnetic latitudes. We have conducted simultaneous observations of CNA at these stations since October 2017. Here we focus on seven substorms during a geomagnetic storm 25–28 August 2018 and study the spatio-temporal development of the global distribution of CNA during these substorms. For all seven substorms, some stations observed CNA enhancements after the substorm onsets. In five cases, the CNA enhancements started around midnight and expanded eastward. The other two cases show westward and anti-sunward development of CNA. The eastward expansion of CNA indicates the eastward drift of high-energy electrons, which is the source of the CNA, due to gradient and curvature drift in the geomagnetic field. The westward expansion of CNA may correspond to westward expansion of the substorm injection region due to dawn-to-dusk electric fields. These results indicate that spatio-temporal development of CNA at subauroral latitudes corresponds to high energy electron drift in the inner magnetosphere.

Plain Language Summary The inner magnetosphere contains plasma particles with a wide range of energies. High-energy electrons (>30 keV) in the inner magnetosphere are accelerated and lost while rotating longitudinally around the earth. They cause satellite failures and astronaut exposure. It is important to study high-energy electrons and understand the dynamics of electrons in the inner magnetosphere for safe space utilization and space weather forecasting. The electron density in the ionosphere, which is enhanced by the precipitation of these high-energy electrons, has been inferred using sensitive ground-based radio receivers called riometers as an increase in cosmic radio noise absorption (CNA). However, there have been few studies of cosmic radio noise absorption (CNA) observations at multi-point stations distributed in longitude to show how this takes place on a global scale. In this study, we investigated the longitudinal extent of CNA using simultaneous riometer observations at six stations at subauroral latitudes in Canada, Alaska, Russia, and Iceland, focusing on the 25–28 August 2018, geomagnetic storm. Our results show that CNA enhancements started around midnight and expanded both eastward and westward around the Earth. Electrons are known to systematically drift in the inner magnetosphere and we discuss the propagation of CNA by considering that.

1. Introduction

Energetic electron precipitation into the high-latitude atmosphere is an important aspect of space weather research and has received much attention in recent years. Magnetospheric substorms are known to inject electrons and ions of wide energy ranges into the nightside inner magnetosphere and the auroral ionosphere (Birn et al., 1997;

Resources: Kazuo Shiokawa, Yoshimasa Tanaka, Mitsunori Ozaki, Akira Kadokura, Shin-ichiro Oyama, Alexey Oinats, Dmitry Baishev
Software: Yuto Kato, Kazuo Shiokawa
Supervision: Kazuo Shiokawa
Validation: Yuto Kato, Kazuo Shiokawa
Visualization: Yuto Kato
Writing – original draft: Yuto Kato
Writing – review & editing: Kazuo Shiokawa, Yoshimasa Tanaka, Mitsunori Ozaki, Akira Kadokura, Shin-ichiro Oyama, Alexey Oinats, Martin Connors, Dmitry Baishev

Wing et al., 2013). This increase in energetic particles and its effect on the atmosphere has been widely studied by ground-based and satellite-based observations (e.g., Arnoldy, 1974; Sotirelis et al., 2013).

Low-energy electrons (<30 keV) precipitating to the ionosphere are absorbed in the E and F regions of the ionosphere and sometimes cause spectacular optical auroral emissions at altitudes around 100 km. The low-energy electrons also enhance the auroral electrojet current, which can be detected by ground-based magnetometers. High energy electrons (>30 keV) can penetrate to altitudes below 90 km without causing significant optical emissions (Baker et al., 1982; Wilson & Stoker, 2002). The substorm-associated electron density enhancement in Earth's lower ionosphere (the D-region) has been inferred using ground-based riometers as an increase in cosmic radio noise absorption (CNA) of radio waves (cosmic noise) originating in galaxies and radio stars (Hargreaves, 1969). It is known that as the electron density in the ionosphere increases due to electron precipitation, the collisions between electrons and the atmosphere become more active, and thus, the cosmic noise is attenuated and the amount of the CNA increases. Therefore, CNA is a method to indirectly identify ionization in the D region ionosphere.

It is well known that CNA occurs in association with auroral and magnetospheric substorms. Kellerman and Makarevich (2011) used CNA obtained from the Kilpisjärvi imaging riometer in Finland and substorm onsets identified by IMAGE satellite auroral images to determine the position of energetic particle precipitation relative to substorm initiation longitudes. They found that the location of CNA occurrence depends on the substorm onset location, and the greater the distance between the observation point and the onset location, the greater the delay of the CNA onset. It is also noted that when the observation point is close to the substorm onset location, the CNA occurs 1∼5 min prior to the substorm onset. Behera et al. (2015) performed a multiple case analysis of CNA events at the Maitri station in Antarctica located at $L = 5$. They found that CNA events at high latitudes were located in the magnetic local time (MLT) range of 23–05 hr during substorms. They also found that the intensity of the CNAs was very well correlated with solar wind speed, interplanetary magnetic field (IMF) B_z, and corresponding eastward component of the interplanetary electric field (IEF) E_y. Behera et al. (2016, 2017) showed that CNAs were found to occur not only on the night side, but also on the noon and evening sides. Recently, Thomas et al. (2022) have statistically shown using conjugate observations between the Arase satellite and ground riometers over Finland that during ground CNA events, Arase observed elevated electron flux in the medium energy range (2–100 keV) and plasma wave activity in the whistler-mode frequency range (0.5–3 kHz) of the spectra.

Multi-point observations of CNAs are necessary to clarify the spatio-temporal development of high-energy particle precipitation (Berkey et al., 1974; Grandin et al., 2017; Kavanagh et al., 2007; Ranta et al., 1981; Rosenberg & Dudeney, 1986; Spanswick et al., 2007). Rosenberg and Dudeney (1986) reported the dependence of CNA on substorm, local time, and season statistically using a one-year data set obtained at the Siple and Halley stations located in Antarctica at $L = 4$. This was the first study of CNA using two ground stations. Spanswick et al. (2007) studied the radial and azimuthal extent of dispersionless electron injection using the Canadian NORSTAR (NORthern Solar Terrestrial ARray) riometer and the CRRES MEB (Combined Release and Radiation Effects Satellite Medium Energy B) particle detector. They found that the initial electron injection region must have a radial extent of less than 1 Earth radius and is capable of having an azimuthal extent of at least 1 hour of local time. Grandin et al. (2017) measured energetic particle precipitation from 95 solar wind high-speed streams (HSS) that occurred in 2006–2008 in a Finnish riometer chain deployed latitudinally at $L = 3.8$–5.7. Their results showed that CNAs occurred frequently and extended to subauroral latitudes when the HSS lasted more than one day. Berkey et al. (1974) studied the development of auroral absorption during substorms on a global scale using 40 high-latitude stations for 60 substorm events, in which the activity begins near magnetic midnight at a magnetic latitude near 65° and then spreads to higher and lower latitudes as well as eastward and westward. Ranta et al. (1981) observed a progression of absorption onset in 13 cases using 43 globally distributed stations. In 6 cases the onset of sharp enhancements in the absorption progressed westward. In 4 cases the absorption onset progressed eastward, and in 3 cases the progression was both eastward and westward.

Although previous observations have revealed the development of high-energy electron precipitation, spatio-temporal development of the global distribution of CNA associated with substorms is not well understood, particularly at subauroral latitudes. In this study, we focus on a magnetic storm that occurred 25–28 August 2018, to analyze the longitudinal spatial-temporal development of CNAs during storm-time substorms for the first time by using six ground-based riometer stations distributed globally at subauroral latitudes at L ∼ 4. Previous multi-point studies of CNA have focused on CNA development mainly in the auroral zone. During geomagnetic

Table 1
Riometer Stations and Their Locations and Start Date of Observation

Station	Abbr.	Geolat (N)	Geolon (E)	Maglat (N)	Maglon (E)	L-value	Start date
Athabasca	ATH	54.60	246.36	61.5	308.3	4.4	25 Oct 2016
Kapuskasing	KAP	49.39	277.81	59.0	353.4	3.8	24 Feb 2017
Husafell	HUS	64.67	338.97	64.9	66.5	5.6	20 Mar 2017
Istok	IST	70.03	88.01	65.9	162.6	6.0	29 Oct 2017
Zhigansk	ZGN	66.78	123.37	61.9	195.7	4.5	27 Sep 2017
Gakona	GAK	62.39	214.78	63.2	271.0	4.9	9 Jan 2017

storms, CNA expands more to subauroral latitudes, as manifestation of dynamical variations of high-energy electrons in the inner magnetosphere. Thus, our six riometer stations at subauroral latitudes are suitable for studying spatio-temporal CNA development during storm-time substorms related to the high-energy electron dynamics in the inner magnetosphere.

2. Instruments

We have conducted simultaneous continuous observations of CNA using broad-beam riometers installed at six ground stations to estimate the longitudinal development of CNA. The stations are located at Athabasca (ATH) and Kapuskasing (KAP) in Canada, Husafell (HUS) in Iceland, Istok (IST) and Zhigansk (ZGN) in Russia, and Gakona (GAK) in Alaska, as shown in Table 1. These stations are located within 59°–66° north magnetic latitude, surrounding the magnetic north pole. The broad-beam riometers were installed by the PWING (study of dynamical variation of Particles and Waves in the INner magnetosphere using Ground-based network observations; http://www.isee.nagoya-u.ac.jp/dimr/PWING/) project (Shiokawa et al., 2017). The broad-beam riometer is made by La Jolla Sciences with an operating frequency of 30 MHz and a frequency bandwidth of 250 kHz. The riometer has dual half-wave dipole antennas with a separation of 14 feet (4.27 m) at more than 60 inches (1.52 m) above the ground. The riometer records the intensity of radio waves at a frequency of 30 MHz coming from galaxies and radio stars with a sampling rate of 64 Hz. The half-power beam width of the riometer is about 60°. In this study, we first analyzed the riometer data for a five-month period from May to September 2018. Although the PWING project started in 2016 to deploy riometers on global scale, this five-month period is the only interval when all six-station riometers were in operation, because some riometers had troubles with instruments, A/D converters, and/or environmental noise. During these five months, we focus on the geomagnetic storm of August 25–28 2018, which is the only storm for which all six stations provided meaningful data (except for ATH and KAP for the first two days). Thus, this storm is really a unique opportunity to examine the CNA development on global scale at subauroral latitudes using all six stations. During this storm, clear CNAs were identified in association with seven substorms. Magnetic storm development and decay, was evaluated using the Dst index available from the Kyoto World Data Center (http://wdc.kugi.kyoto-u.ac.jp/aeasy/index.html).

Table 2
Magnetometer Stations and Their Locations Used in This Paper

Station	Geolat (N)	Geolon (E)	Maglat (N)	Maglon (E)
Honolulu (HON)	21.3	202.0	20.9	270.9
Fresno (FRN)	37.1	240.3	42.6	305.1
Boulder (BOU)	40.1	254.8	48.5	321.3
Bay St Louis (BSL)	30.4	270.4	40.7	342.1
San Juan (SJG)	18.1	293.9	26.8	11.9
San Fernando (SFS)	36.7	354.1	27.1	70.5
Surlari (SUA)	45.3	26.3	40.2	99.9
Alma Ata (AAA)	43.3	76.9	38.8	150.2
Lanzhou (LZH)	36.1	103.9	30.6	177.3
Kakioka (KAK)	36.2	140.2	29.1	213.0

In order to determine the MLT range and universal time of substorm onset, we used magnetic field data obtained from ground-based magnetometers and the SMU/SML index provided by SuperMAG (https://supermag.jhuapl.edu/). SuperMAG is a worldwide collaboration of organizations and national agencies that currently operate more than 300 ground-based magnetometers. Table 2 shows the abbreviations, geographic coordinates, and geomagnetic coordinates of the ground-based magnetometer stations used in this study. Figure 1 shows the PWING ground-based stations and the ground-based magnetometer stations used in the present analysis. These stations were located at 20°N–50°N magnetic latitudes. The substorm onset MLT range was estimated from the MLT range of the reversal of the zonal (east-west) component of the mid-latitude magnetic field variation (Clauer & McPherron, 1974). The SMU/SML index was calculated from the maximum

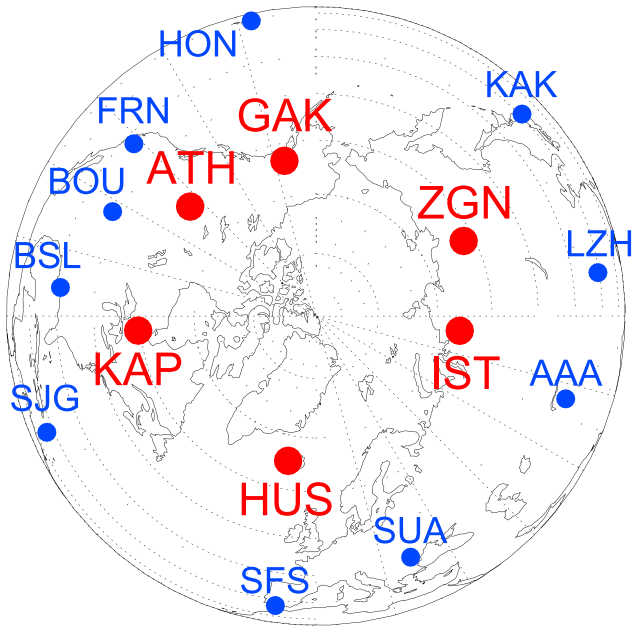

Figure 1. The MLAT and MLT map of PWING stations (red) and magnetometer stations (blue).

auroral electrojet intensity at stations with magnetic latitudes of 40°N–80°N (Gjerloev, 2012; Newell & Gjerloev, 2011).

The wave and planetary (Wp) index (https://www.isee.nagoya-u.ac.jp/~nose.masahito/s-cubed/) developed by Nosé et al. (2012) was used to determine more accurate timing of the substorm onsets. This index is derived from wave power of low-latitude Pi2 pulsations. It is well-known that pulsations of this type are clearly observed at mid- and low-latitude ground stations on the nightside at substorm onset. Therefore, with 1-s data from multiple stations distributed in longitude around the Earth's circumference, substorm onset can be regularly monitored. To examine the CNA in relation to interplanetary space parameters, we also used IMF and solar wind parameters provided by the OMNIWeb (http://omniweb.gsfc.na-sa.gov/form/omni_min.html; King and Papitashvili (2005); Papitashvili and King (2020)).

The radio wave intensity received by a riometer undergoes diurnal variation with a period of one sidereal day due to the rotation of the earth under the cosmic noise sources. When the geomagnetic activity is quiet, this diurnal variation becomes dominant as the output voltage of the riometers and is called the Quiet Day Curve (QDC). When the electron density in the lower ionosphere increases due to high-energy electron precipitation from the magnetosphere, the radio waves are partially absorbed mainly in the ionospheric D region. In this case, the output voltage of the riometer decreases from the value of the diurnal variation. The amount of radio wave absorption is measured as the integral of the amount of absorption at each altitude along the propagation path. The absorption of these radio waves is positively correlated with the electron density in the lower ionosphere and varies with the collision frequency of electrons and neutral particles. In the case of a riometer measuring 30 MHz radio waves, the height-resolved CNA peaks around 90 km altitude (Tanaka et al., 2007; Turunen et al., 2009). Thus, we can estimate the amount of ionization at an altitude of 90 km due to high-energy electron precipitation using a riometer as the attenuation of output voltage relative to the QDC. The absorption (CNA) is given by the following equation (Armstrong et al., 1977).

$$\mathrm{CNA}(dB) = -10 \cdot \log_{10}\left(\frac{V_{\mathrm{OUT}}}{\mathrm{QDC}}\right) = 10 \cdot \left(\log_{10}(\mathrm{QDC}) - \log_{10}(V_{\mathrm{OUT}})\right),$$

where V_{OUT} represents the output voltage of the riometer. The QDC was determined every 1 s as the 70th percentile of the 1984 (64 Hz × 31 days) data points of the output voltages for ± 15 days before and after the day of observation (31 days in total) (Shiokawa et al., 2017).

3. Results

Figure 2 shows variations of IMF B_z, solar wind flow speed, solar wind proton density, Dst index, SMU/SML index, and CNA at the six stations for the 4 days from 25 August 2018, during a strong geomagnetic storm. The IMF B_z shows a decrease starting at ∼15 UT on August 25, which is consistent with the sharp decrease in Dst and SML indices. The solar wind velocity increased from ∼9 UT on August 26 and reached about 650 km/s. The proton density fluctuated sharply and reached ∼30 cm^{-3} on August 26, but it did not fluctuate sharply after August 27 and remained stable at ∼5 cm^{-3}. The Dst index decreased to −175 nT at about 07 UT on August 26, indicating that a strong magnetic storm occurred. Figure 2e shows that around the end of the main phase of the magnetic storm, a large substorm with SML index less than −2000 nT was observed, while during the recovery phase, seven substorms with values less than −1000 nT were observed. In this study, we focus on these seven substorms (indicated by arrows) during the recovery phase of the storm. We have not discussed some substorms in which there were no CNA enhancements at any of the stations, as we believe that the CNA signature was masked by the preceding substorm. Associated with the chosen substorms, we can see CNA enhancements at several stations.

Figures 3–5 show the SMU/SML index, Wp index, zonal component of the magnetic field, and CNA for three substorm events. The remaining four substorm events are listed in Supporting Information S1 (Figures S1, S2, S3,

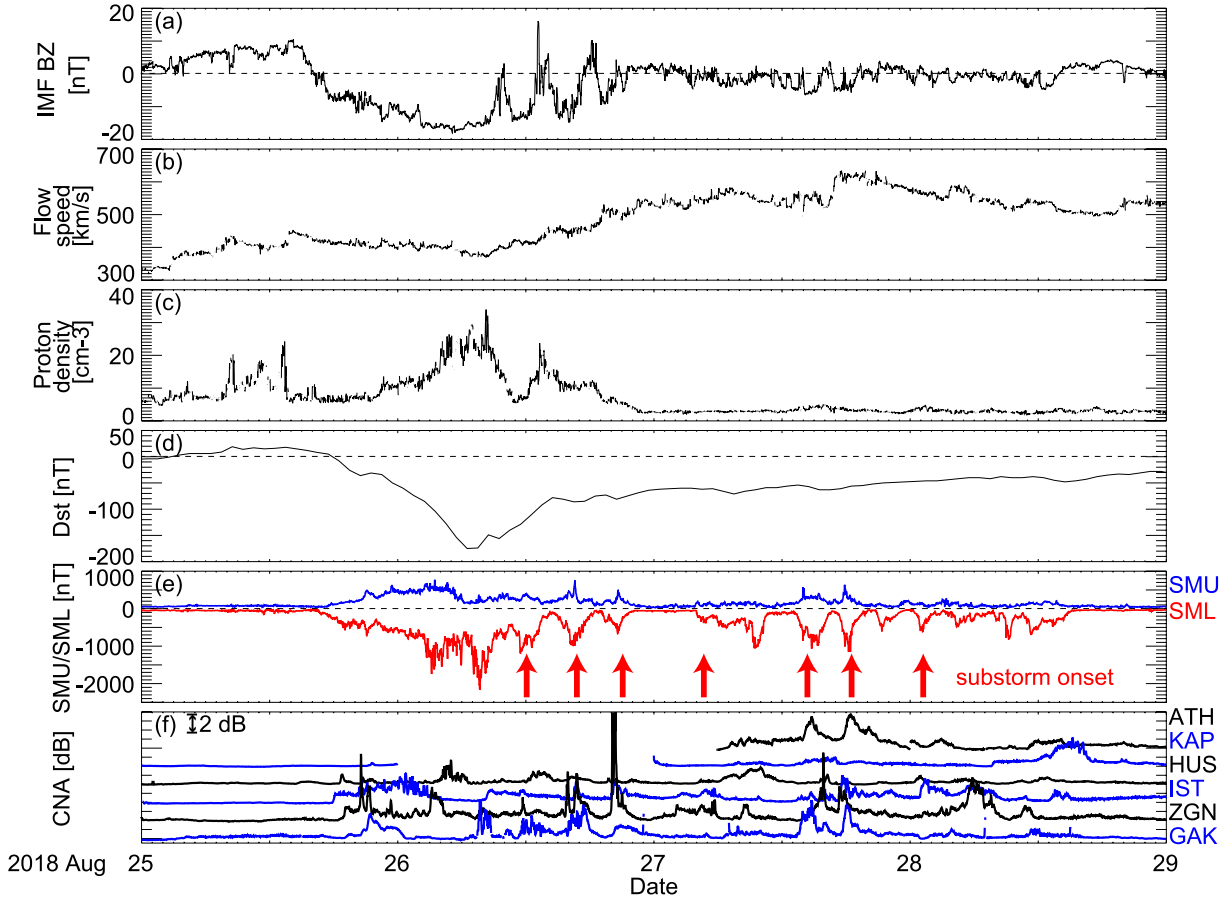

Figure 2. The variations of (a) IMF B_z, (b) solar wind flow speed, (c) solar wind proton density, (d) Dst index, (e) SMU and SML indices, (f) CNA intensity at ATH, KAP, HUS, IST, ZGN, GAK during a strong magnetic storms on August 25–28, 2018. In (e), red arrows show seven substorms with decreases of SML index during the storm recovery phase.

and S4). On the right side of panels showing the zonal component of the magnetic field, the MLTs of the stations at the time of substorm onset are shown. For the substorms No.1 to No.4, we used CNA data at Meanook (MEA, MLAT: 62.05°N, MLON: 305.76°E) which is 21 km east of ATH, because CNA data were not available at ATH in this period. The riometer at MEA is a 30-MHz broad-beam riometer similar to those of PWING. Similarly, for the CNA panels, the UTs and MLTs of the stations at the times (red arrows) of CNA onset are given. The following criteria were defined to identify CNA onset time t_0: (a) $\frac{dCNA}{dt}$ is larger than 0.04 [dB/min] at $t = t_0$, (b) CNA should reach a value of 0.25 dB above CNA(t_0), and (c) the CNA rise time to the maximum is less than 30 min Figure 6 schematically shows the longitudinal development of CNAs and the substorm onset MLT range inferred from Figures 3–5, Figures S1, S2, S3, and S4 in Supporting Information S1. The velocities in the figure indicate propagation velocities of CNA in the source plasma at $L = 4.9$ (left) and in the ionosphere (right). We defined substorm onset MLT range, shown by blue curves in Figure 6, as the MLT of the reversal of zonal component of the magnetic field in Figures 3–5 and Figures S1, S2, S3, and S4 in Supporting Information S1, by considering the zonal magnetic field variations caused by substorm current wedge (Clauer & McPherron, 1974). It should be noted that the longitudinal width of the blue curve is not the width of the substorm current wedge, but the longitudinal difference of two ground stations where the zonal component reversal of magnetic field was observed.

First, we discuss the substorm No. 6 in Figures 3a–3d, which is characterized by eastward CNA expansion. From Figures 3a and 3b, we can see that the substorm onset time is 1713 UT, as indicated by the vertical dashed line in the figure. From the variation of the zonal magnetic field in Figure 3c, the substorm onset MLT range is inferred as 2231–0007 MLT, as the boundary MLT of positive and negative responses of zonal magnetic field variations (Clauer & McPherron, 1974). The red arrows in Figure 3d indicate the onset timings of CNA enhancements. The CNA enhancements started almost simultaneously at IST at 2316 MLT (1716 UT) and ZGN at 0102 MLT

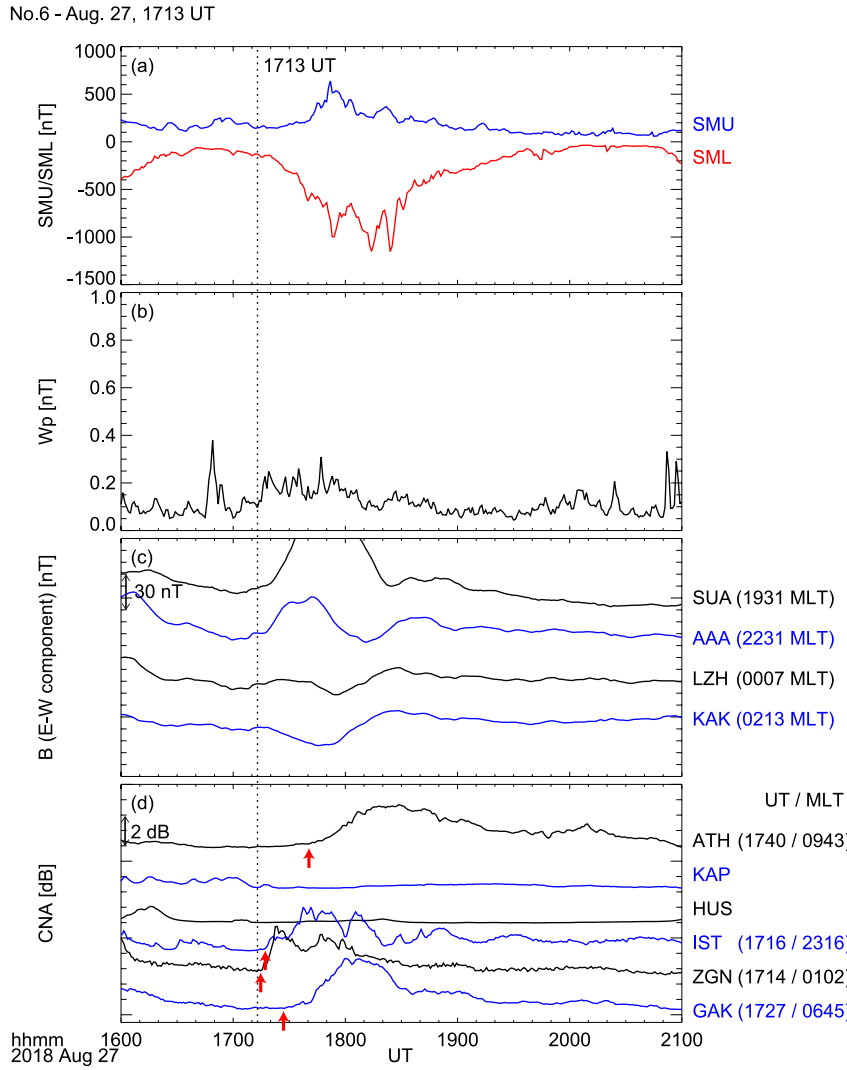

Figure 3. From top to bottom, (a) SMU and SML index, (b) Wp index, (c) zonal component of low-latitude magnetic fields, and (d) CNAs at ATH, KAP, HUS, IST, ZGN, GAK over 5 hr for the substorm No.6. On the right side of the panels of zonal component of the magnetic field, the MLTs of the stations at the timing of substorm onset are represented. On the right side of CNA panels, the UTs and MLTs of the stations at the timing of CNA onset are represented. Red arrows show the timing of CNA onset at each station. Vertical dashed line shows substorm onset time.

(1714 UT), which may suggest that the CNA start MLT range has a finite extent in longitudes. We can see that the CNAs increase in the order from GAK at 0645 MLT (1727 UT) to ATH at 0943 MLT (1740 UT). Figure 6f shows development of CNAs and the substorm onset MLT range in the polar map from the magnetic north pole. The substorm onset MLT range are shown in blue, the CNA start MLT range in orange, and the ground-based stations with increased CNA are circled in red, with the arrows indicating the direction of spatial expansion. The velocities indicate the propagation velocities of CNA in the source plasma at $L = 4.9$ (left) and in the ionosphere (right). From this figure, we can see that the substorm and CNA start MLT range coincided at night, and the CNA developed eastward from night to dawn.

Next, we discuss the substorm No. 1 in Figures 4a–4d, which is characterized by westward CNA expansion. Figures 4a and 4b show that the substorm onset time is 1121 UT, and Figure 4c shows that the substorm onset MLT range is 2021–0021 MLT. Figure 4d shows that CNA enhancement started almost simultaneously at MEA at 0311 MLT (1121 UT) and at GAK at 0039 MLT (1121 UT), IST at 1724 MLT (1124 UT), followed by ZGN at 1921 MLT (1132 UT) and HUS at 1151 MLT (1209 UT). Figure 6a shows that the CNA start MLT range is very wide over ~10 MLT. CNA enhancements occurred nearly simultaneously at GAK and IST, but not at ZGN

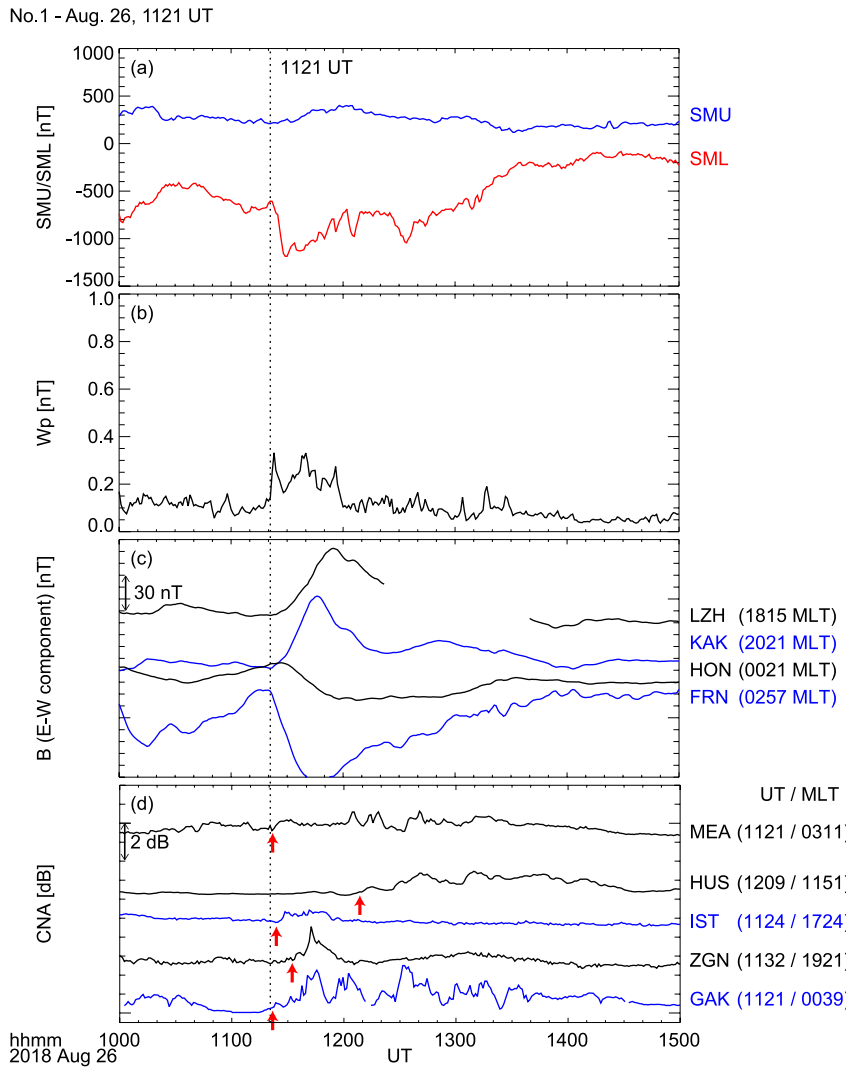

Figure 4. From top to bottom, (a) SMU and SML index, (b) Wp index, (c) zonal component of low-latitude magnetic fields, and (d) CNAs at MEA, HUS, IST, ZGN, GAK over 5 hr for the substorm No.1.

which is located between GAK and IST, possibly because ZGN is slightly at lower latitudes than GAK and IST. The CNA developed westward from night to dusk.

The substorm No. 4 in Figures 5a–5d is characterized by CNA start MLT range in the dayside. In Figures 5a and 5b, the SMU/SML change is small, but from the Wp index, the substorm onset time is definitely 0354 UT, and Figure 5c shows that the substorm onset MLT range is 2154–2336 MLT. In Figure 5d, CNA increases at ZGN at 1142 MLT (0402 UT) first, followed by IST at 1022 MLT (0422 UT), and GAK at 1804 MLT (0446 UT) in that order. Figure 6d shows that the substorm onset MLT range is located on the night side, while the CNA start MLT range is located in the dayside. There is a possibility that the CNA developed anti-sunward from ZGN to GAK and ZGN to IST. From 0520 to 0550 UT, there are two CNA increases simultaneously at IST and ZGN. The variation in CNA and Pc5 shows some similarity, as reported by Motoba et al. (2013). However, the CNA amplitude at GAK is small, so we consider it may not be propagating from the ZGN to the GAK. This event is futher discussed below.

We also briefly introduce the other four cases. For substorm No.2 (Supporting Information S1, Figures S1a, S1b, S1c and 9d), Figure 6b shows eastward CNA expansion from ZGN at 2330 MLT (1542 UT) to GAK at 0512 MLT (1554 UT) and MEA at 0748 MLT (1558 UT). For substorm No. 3 (Figures S2a, S2b, S2c and S2d in Supporting Information S1), Figure 6c shows eastward expansion from HUS at 1919 MLT (1937 UT) to IST at 0158 MLT (1958 UT), ZGN at 0343 MLT (1955 UT), GAK at 0931 MLT (2013 UT) and MEA at 1214 MLT (2024 UT).

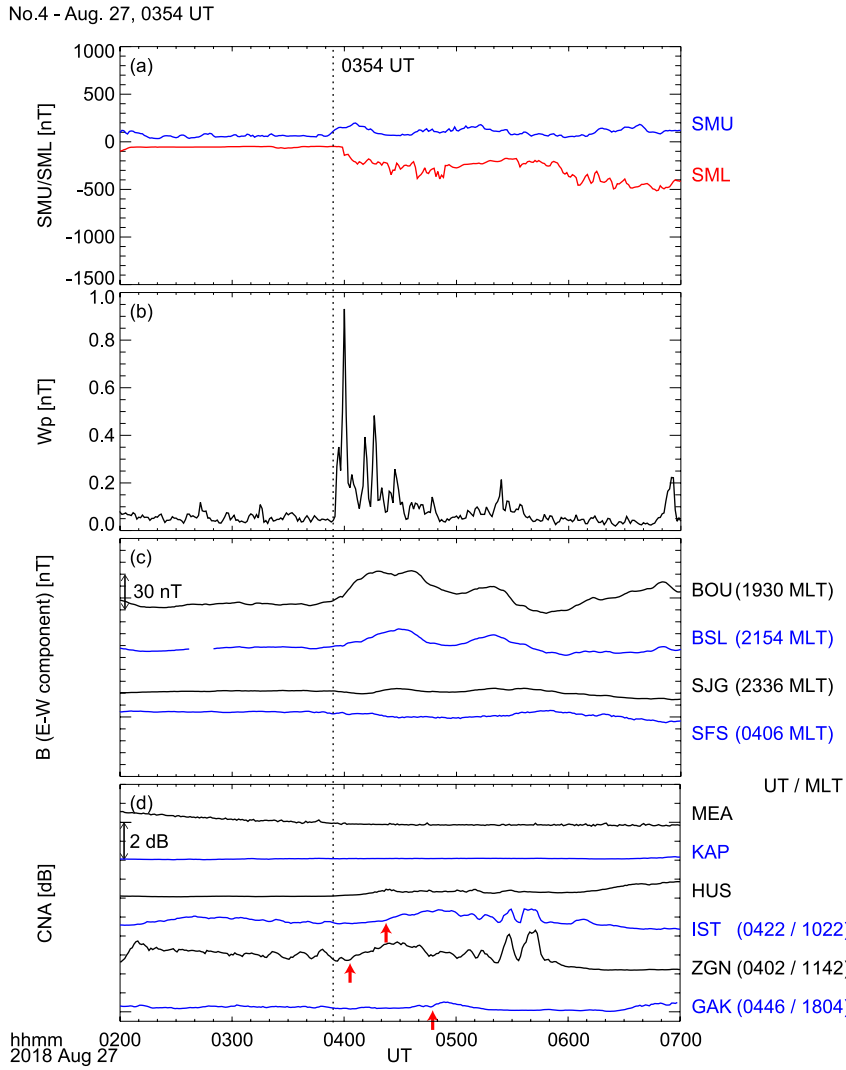

Figure 5. From top to bottom, (a) SMU and SML index, (b) Wp index, (c) zonal component of low-latitude magnetic fields, and (d) CNAs at MEA, KAP, HUS, IST, ZGN, GAK over 5 hr for the substorm No.4.

For substorm No. 5 (Figures S3a, S3b, S3c and S3d in Supporting Information S1), Figure 6e shows eastward expansion from IST at 1944 MLT (1344 UT) and GAK at 0255 MLT (1337 UT) to ATH at 0551 MLT (1357 UT). For substorm No. 7 (Figures S4a, S4b, S4c and S4d in Supporting Information S1), Figure 6g shows eastward expansion from HUS at 0009 MLT (0027 UT) to IST at 0654 MLT (0054 UT) and ZGN at 0855 MLT (0107 UT).

These seven substorm events are summarized in Table 3. The substorm onset MLT range is around midnight for all substorms. This result is consistent with Frey and Mende (2006) which reported using the global auroral images obtained by the IMAGE satellite that the average MLT of the substorm onsets is 2250 ± 0127 hr. The CNA start MLT range are nightside for the six of the seven cases except for No. 4 which is in dayside. The directions of expansion are eastward for the five of the seven cases, one is westward, and the other one is eastward or anti-sunward.

4. Discussion

When high-energy electrons precipitate into the ionosphere, a variety of effects are observed depending on their energy. The westward auroral electrojet current is associated with auroral electrons precipitating into the E-region, and higher energy electrons cause absorption of cosmic radio noise in the D-region (Baker et al., 1982; Wilson & Stoker, 2002). In this study, we searched for substorms during the storm of 25–28 August 2018, using the SMU/SML index, which is calculated from the maximum auroral electrojet current intensity, and investigated

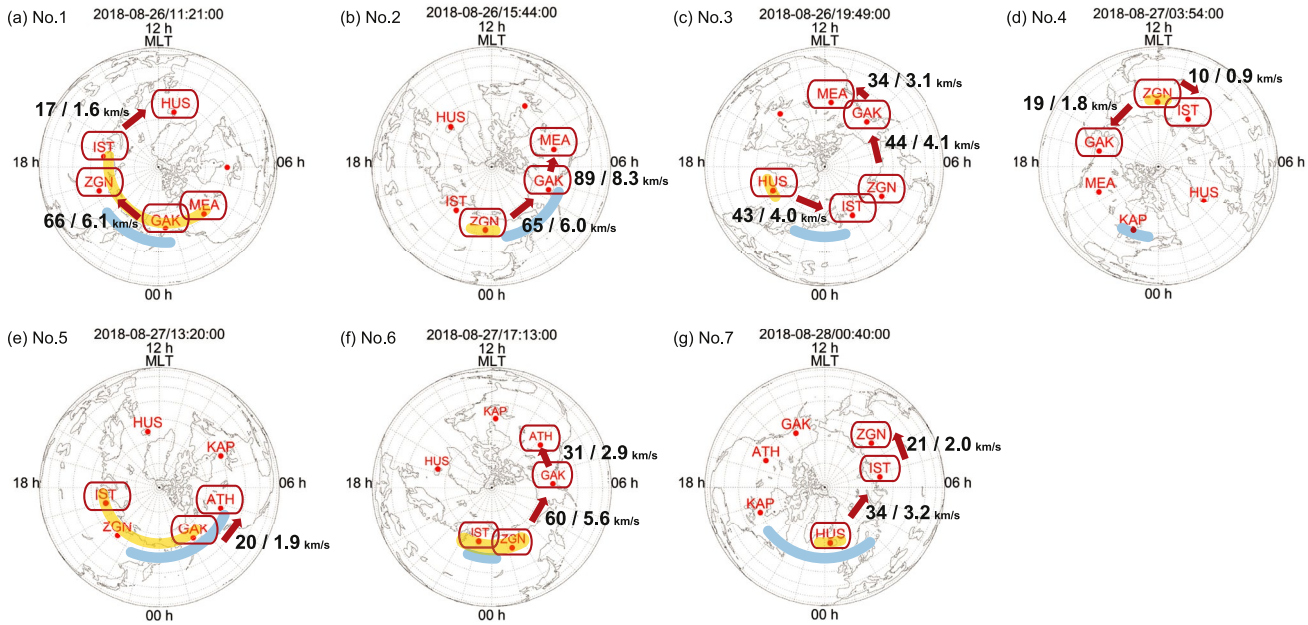

Figure 6. The longitudinal development of CNAs and the substorm onset MLT range for the seven substorm events. The substorm onset MLT range are shown by blue line, the CNA start MLT range by orange line, and the ground-based stations with increased CNA are circled in red, with the arrows indicating the direction of CNA expansion. The velocities indicate the propagation velocities of CNA in the source plasma at $L = 4.9$ (left) and in the ionosphere (right).

the spatio-temporal relationships of the increased CNA after the substorm onsets for seven of them. The results showed that the substorm onset MLT ranges coincided with the CNA start MLT range in five out of seven cases. The fact that substorm onset MLT range are found on the nightside is consistent with the statistical results of auroral substorm onset from the IMAGE satellite (e.g., Frey & Mende, 2006). It is also consistent with previous studies that substorm-related CNAs occur at midnight (Behera et al., 2015; Kellerman & Makarevich, 2011). High-energy electrons injected into the inner magnetosphere by substorms may directly collide with the atmosphere and cause CNAs on the night side. At local times away from nightside, pitch-angle scattering of high-energy electrons caused by wave-particle interactions may play an important role in causing CNAs. Therefore, it is also necessary to clarify the relationship of CNA with magnetospheric ELF/VLF waves (e.g., Ozaki et al., 2009; Shiokawa et al., 2014). Magnetospheric chorus waves in the upper band and lower band frequencies resonate with electrons in a wide energy range (Ozaki et al., 2022), so the comparison between the longitudinal development of the ELF/VLF wave activity (Takeshita et al., 2019; Yonezu et al., 2017) and CNA would be important future work. Kellerman and Makarevich (2011) reported that the CNA increases during the growth phase of the substorm, that is, before the substorm onset. In this study, events No. 3 and 7 show CNA increases at HUS just before the substorm onset. This may be related to small injections (auroral pseudo-breakups) in the nightside magnetosphere during substorm growth phase (Hsu & McPherron, 2007; Koskinen et al., 1993; Shiokawa et al., 1996). For substorm No.3, the Wp index shows that the Wp index increased at the same time as the start of

Table 3
List of Seven Substorms With Their Onset Magnetic Local Time (MLT), CNA Start MLT Range, and Expansion Direction of CNA

No.	Substorm onset time [UT]	Substorm onset MLT range [MLT]	CNA start MLT range [MLT]	Expansion direction
1	26 Aug. 1121	2021–0021	MEA[0311], GAK [0039], IST [1724]	Westward
2	26 Aug. 1544	0044–0444	ZGN [2330]	Eastward
3	26 Aug. 1949	2207–0107	HUS [1919]	Eastward
4	27 Aug. 0354	2154–2336	ZGN [1142]	Anti-sunward
5	27 Aug. 1320	2220–0456	IST[1944], GAK [0255]	Eastward
6	27 Aug. 1713	2231–0007	IST [2316], ZGN [0102]	Eastward
7	28 Aug. 0040	2022–0258	HUS [0009]	Eastward

the increases in HUS (~1932 UT). For substorms No.7, the Wp index increased slightly at the same time as the start of the increases in HUS (~0022 UT).

Next, we discuss the results of five of the seven cases in which the CNA developed eastward on the dawn side. This can be due to the eastward drift of high-energy electrons in the inner magnetosphere caused by the gradient B and curvature drifts. In addition, the sunward $\mathbf{E} \times \mathbf{B}$ drift due to the dawn to dusk convection electric field also contribute to the eastward drift on the dawn side. Figure 6 shows the longitudinal drift velocities of high energy electrons in the magnetosphere estimated from the time difference of CNA start at neighboring stations for an average L value of the six stations ($L = 4.9$). From Figure 6, we can see that the velocity of eastward expansion there is 20–89 km/s. The gradient B drift velocity $\boldsymbol{v_G}$ is given by $\boldsymbol{v_G} = \frac{mv_\perp^2}{2qB^3}(\boldsymbol{B} \times \nabla \boldsymbol{B})$, the curvature drift velocity $\boldsymbol{v_R}$ is given by $\boldsymbol{v_R} = \frac{mv_\parallel^2}{qB^3}(\boldsymbol{B} \times \nabla \boldsymbol{B})$, so eastward drift velocity $\boldsymbol{v_B}$ is given by $\boldsymbol{v_B} = \boldsymbol{v_G} + \boldsymbol{v_R} = \frac{m}{qB^3}\left(v_\perp^2 + \frac{1}{2}v_\parallel^2\right)(\boldsymbol{B} \times \nabla \boldsymbol{B})$ (m: electron mass, q: elementary charge, B: magnetic field) (Nicholson, 1983). For substorm No.2 (Figure S1 in Supporting Information S1), from ZGN (1542 UT/2330 MLT) to GAK (1554 UT/0512 MLT), the MLT difference is 342 min (0512–2330 MLT) and timing difference is 12 min. Thus the CNA velocity at $L = 4.9$ can be estimated as $2\pi \mathrm{Re} \times 4.9 \times (342/1440)/(12 \times 60) = 65$ km/s. The CNA velocity at a 90 km altitude is estimated as $2\pi(\mathrm{Re} + 90) \times \cos\theta \times 342/1440 = 6.0$ km/s for $\theta = 63.3°$ which is an average latitude of the stations. Assuming that $L = 4.9$ and a simple dipole magnetic field B, we obtained 20 km/s at an energy of 37 keV and 89 km/s at an energy of 164 keV, very similar values to those inferred from observations. This indicates that electrons in a wide range of energies were expanding eastward and precipitating into the D-region ionosphere.

In one of the seven cases (substorm No. 1), the CNA developed westward on the dusk side. It is possible that the electrons drifted westward in the evening side due to the $\mathbf{E} \times \mathbf{B}$ drift in the sunward direction. The $\mathbf{E} \times \mathbf{B}$ drift velocity $\boldsymbol{v_d}$ is given by $\boldsymbol{v_d} = \frac{E \times B}{B^2}$. We calculated the westward drift velocity of 17 km/s in Figure 4 from the time difference of CNA enhancement at IST and HUS. This velocity corresponds to the electric field of 4.5 mV/m in the dipole field at $L = 4.9$. The background eastward drift by gradient and curvature of magnetic field discussed above (~20 km/s) would further increase the values of necessary electric field to ~10 mV/m to cause the observed westward drift. This value is about an order of magnitude larger than the normal average magnetospheric dawn-to-dusk electric field (e.g., 50 kV/20 Re = 0.4 mV/m, Boyle and Reiff (1997)). According to the in-situ measurements of electric field by the Akebono satellite by Nishimura et al. (2006), strong electric field appears between $L = 2$ and $L = 6$ in both dawn and dusk sectors with the magnitude from 2 to 4 mV/m during the main phase of geomagnetic storms. But this value seems to be smaller than the required electric field (~10 mV/m) to explain the present observation of westward CNA development. Another possibility may be the $\mathbf{E} \times \mathbf{B}$ drift by intense poleward electric field associated with subauroral ion drift (SAID). The expansion velocity of the IST and HUS is 1.6 km/s, which is comparable with the $\mathbf{E} \times \mathbf{B}$ drift speed seen in the SAID (e.g., Maynard, 1978; Smiddy et al., 1977; Spiro et al., 1979). We should note that the SAID plasma drift velocity is for ionospheric low-energy electrons which would be different from the drift velocities of energetic electrons in the magnetosphere. As the other possibility, Kellerman and Makarevich (2011) reported that the westward expansion may be not due to electron drift, but due to the longitudinal expansion of the injection region of electrons. Kennel (1969) reported westward expansion of auroral absorption caused by penetration of hot electron from the tail into the inner magnetosphere over the entire width of tail. If the injection region has a dawn-dusk extent, their consequences of precipitation of these particles into the ionosphere could expand longitudinally.

In Figure 6, the eastward velocities of 20–89 km/s in the magnetosphere are estimated from the observed eastward CNA expansion velocities of 1.9–8.3 km/s in the ionosphere at an altitude of 90 km, based on the timing difference of the CNA onsets. Similarly, the westward velocities of 17–66 km/s in the magnetosphere corresponds to 1.6–6.1 km/s in the ionosphere. Berkey et al. (1974) reported that the eastward/westward expansion velocities of the auroral absorption are 0.7–7 km/s and ~1 km/s, respectively, in the ionosphere. Ranta et al. (1981) reported that the expansion velocity of the sharp onset of auroral absorption toward the east as 0.4–9 km/s and toward the west as 1–31 km/s. These velocities in previous studies are comparable to the values in this study. These previous observations were made mainly in the auroral zone, while the present observations were made at subauroral latitudes. The particle drift velocities are proportional to the energy of the particles and inversely proportional to the magnetic field intensity [for example, Nicholson, 1983; Chisham, 1996]. At subauroral latitudes, electron energies will be larger, while the magnetic field intensity is stronger, compared with those at auroral latitudes. This may be the reason why we obtained the comparable eastward velocities between present and previous studies.

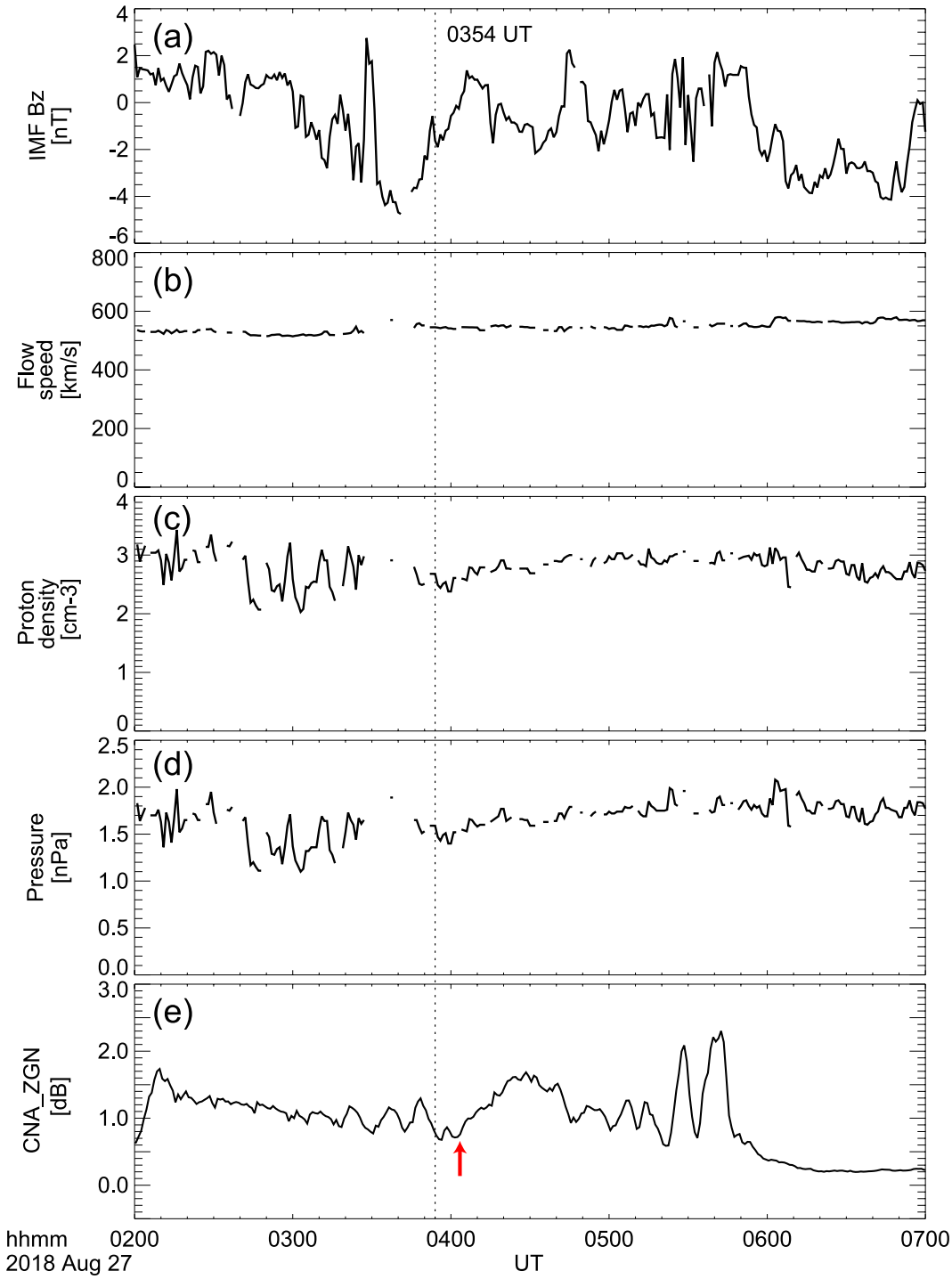

Figure 7. From top to bottom, (a) IMF B_z, (b) solar wind flow speed, (c) solar wind proton density, (d) solar wind pressure, and (e) CNA intensity at ZGN for 5 hr for the substorm No.4 when the CNA enhancement started from dayside.

Next, we discuss the anti-sunward expansion seen in substorm No. 4. From Figures 5 and 6d, the MLT range where the CNA started was on the dayside and the CNA did not increase at the MEA, KAP, and HUS in the nightside. These facts suggest that the CNA enhancement is not due to substorm-associated particle injection from the nightside. Figure 7 shows the IMF B_z, solar wind flow speed, solar wind proton density, solar wind pressure, and CNA at ZGN for the period of the substorm No. 4. From this figure, there are no clear changes in solar wind parameters that correspond to the CNA enhancement at ZGN. It is not likely that the electrons on

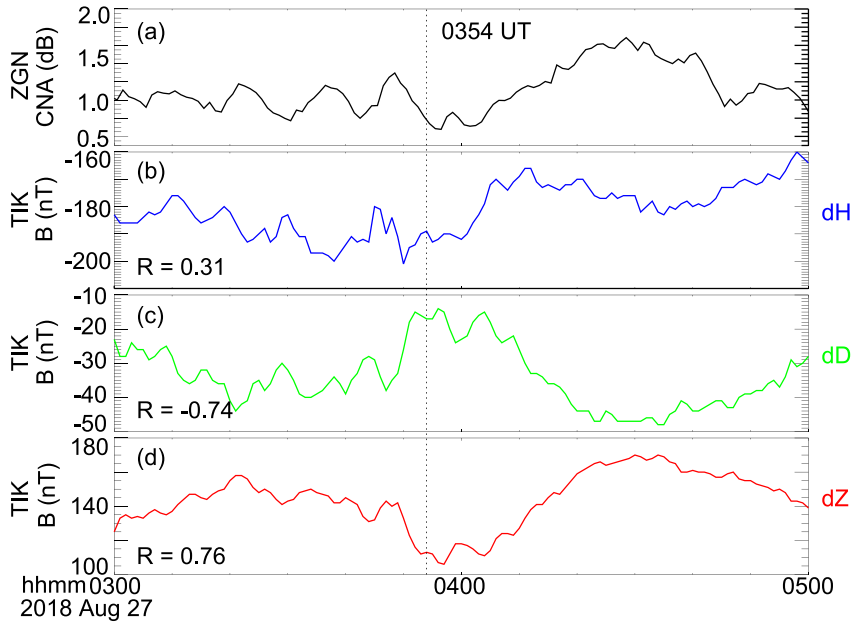

Figure 8. (a) CNA, (b) H-, (c) D-, and (d) Z-component of the ground magnetometer data from Tiksi (TIK, MLAT: 66.4°N, MLON: 198.4°E) station. Correlation coefficients between CNA intensity and three component of magnetometer data are shown to the left of each panel, respectively.

the noon side were precipitated by a sudden increase of solar wind. Figure 8 shows CNA at ZGN, and H-, D-, and Z-component of the ground magnetometer data from Tiksi (TIK, MLAT: 66.4°N, MLON: 198.4°E) station over 2 hr. We show the correlation coefficients between CNA intensity and three component of magnetometer data to the left of each panel, respectively. TIK is located at about same magnetic longitude as ZGN. From this figure, there is a good correlation between CNA intensity and magnetometer data, suggesting modulation of CNA by geomagnetic pulsations that were seen with periods of 5–20 min before and after the substorm that started at 0354 UT. Spanswick et al. (2005) have shown similar good correlation between Pc5 waves and CNA, and suggested Pc5 wave modulation of high energy electron precipitation in the dayside magnetosphere to cause dayside CNA. The present event may correspond to such a dayside modulation of energetic electron precipitation due to Pc5-range waves.

Finally we should note that no CNA enhancements were found at KAP for the seven substorms discussed here. This can be attributed to the fact that the magnetic latitude of KAP is 59.0 N° (L = 3.8) which is the lowest latitude in the six PWING stations. Thus, the high-energy electrons injected by these seven substorms might not reach the L-shell mapped to KAP.

5. Conclusion

This study attempts to understand the longitudinal development of CNA at subauroral latitudes during seven storm-time substorms on August 25–28, 2018 when all the six PWING ground-based riometer data are available. The results of this study can be summarized as follows.

1. In five cases, there were CNA enhancements after the substorm onset. This suggests that the particle injection associated with a substorm increases the CNA intensity.
2. Five cases show eastward CNA expansion from night to dawn. One case shows westward CNA expansion from night to dusk. The other case shows anti-sunward CNA expansion at dayside.
3. The velocity of eastward expansion of high energy electrons is estimated to be 20–89 km/s. This velocity corresponds to the gradient B and curvature drift velocity of 37–164 keV at L = 4.9 in a dipole magnetic field.

4. The velocity of westward expansion of high energy electrons are 66 km/s and 17 km/s for the two station pairs. The latter velocity corresponds to the E × B drift velocity in E = 4.5 mV/m. The westward expansion of the substorm injection region may also be a cause of this CNA westward expansion.

These results indicate that spatio-temporal development of CNA at subauroral latitudes corresponds to high energy electron drift in the inner magnetosphere.

Data Availability Statement

The CNA data at ATH, KAP, HUS, IST, ZGN and GAK used in this paper are available from the ERG-Science Center operated by ISAS/JAXA and ISEE/Nagoya University (Shiokawa et al., 2023a, 2023b, 2023c, 2023d, 2023e, Shiokawa and Tanaka (2023)). The SMU/SML index and magnetometic field used in this paper were provided by the SuperMAG (Gjerloev, 2012). The solar wind and IMF were provided by the National Aeronautics and Space Administration (NASA) Coordinated Data Analysis Web (CDAWeb) (McComas et al., 2022; Smith & Ness, 2022). The Wp index used in this paper was provided by the World Data Center for Geomagnetism, Kyoto, and M. Nosé (2016). The Dst index used in this paper was provided by the World Data Center-C2, Kyoto University (World Data Center for Geomagnetism, Kyoto, et al., 2015).

Acknowledgments
We express our sincere gratitude to Y. Katoh, H. Hamaguchi, Y. Yamamoto, and T. Adachi of ISEE for their continued technical support. The riometer at ATH, KAP, HUS, IST, ZGN and GAK are operated respectively with local support provided by Athabasca University, Virginia Polytechnic Institute and State University, HUS (University of Iceland), the Institute of Solar-Terrestrial Physics (ISTP) of Siberian Branch of the Russian Academy of Sciences, the Yu.G. Shafer Institute of Cosmophysical Research and Aeronomy (SHICRA) of Siberian Branch of the Russian Academy of Sciences (program of government assignment, registration number 122011700182-1), and Geophysical Institute of University of Alaska Fairbanks, respectively. The CNA data at MEA used in this paper are provided by the Canadian Hazards Information Service, Natural Resources Canada (https://chis.nrcan.gc.ca/index-en.php). We also express our sincere gratitude to Robyn Fiori of Canadian Hazards Information Service, Natural Resources Canada, for providing riometer data at Meanook. We acknowledge use of NASA/GSFC's Space Physics Data Facility's OMNIWeb (or CDAWeb or ftp) service, and OMNI data (King and Papitashvili (2005); Papitashvili and King (2020)). We also acknowledge the SuperMAG collaborators (https://supermag.jhuapl.edu/info/?page=acknowledgement). The database construction for the PWING ground-based instruments is supported by the ERG Science Center (http://ergsc.isee.nagoya-u.ac.jp/) and the IUGONET (Inter-university Upper atmosphere Global Observation NETwork) project (http://www.iugonet.org/). The authors were also supported by the KAKENHI (Grant-in-Aid for Scientific Research; 15H05815, 16H06286, 21H04518, 22H01283, 21KK0059, 21K18651, 22H00173, 22K21345) from the Japan Society for the Promotion of Science. This study was supported by JSPS Bilateral Program (JPJSBP120214805) and Russian Foundation for Basic Research (21-55-50013). The work of SO was carried out by the joint research program of Planetary Plasma and Atmospheric Research Center, Tohoku University. The observatory at Athabasca was constructed and operated with funding from the Canada Foundation for Innovation. M. Connors' research is supported by NSERC.

References

Armstrong, R. J., Berkey, F. T., & Melby, T. (1977). The day to night absorption ratio in auroral zone riometer measurements. *Planetary and Space Science*, *25*(12), 1193–1198. https://doi.org/10.1016/0032-0633(77)90098-8

Arnoldy, R. L. (1974). Auroral particle precipitation and Birkeland currents. *Reviews of Geophysics*, *12*(2), 217–231. https://doi.org/10.1029/RG012i002p00217

Baker, D. N., Hones, E. W., Belian, R. D., Higbie, P. R., Lepping, R. P., & Stauning, P. (1982). Multiple-spacecraft and correlated riometer study of magnetospheric substorm phenomena. *Journal of Geophysical Research*, *87*(A8), 6121–6136. https://doi.org/10.1029/JA087iA08p06121

Behera, J. K., Sinha, A. K., Singh, A. K., Vichare, G., Dhar, A., Labde, S., & Jeeva, K. (2015). Substorm related CNA near equatorward boundary of the auroral oval in relation to interplanetary conditions. *Advances in Space Research*, *56*(1), 28–37. https://doi.org/10.1016/j.asr.2015.03.036

Behera, J. K., Sinha, A. K., Vichare, G., Bhaskar, A. T., Honary, F., Rawat, R., & Singh, R. (2017). Enhancement and modulation of cosmic noise absorption in the afternoon sector at subauroral location (L = 5) during the recovery phase of 17 March 2015 geomagnetic storm. *Journal of Geophysical Research: Space Physics*, *122*(9), 9528–9544. https://doi.org/10.1002/2017JA024226

Behera, J. K., Sinha, A. K., Vichare, G., Kozyreva, O., Rawat, R., & Dhar, A. (2016). Dayside cosmic noise absorption at the equatorward boundary of auroral oval as observed fromMaitri, Antarctica (L = 5; CGM 62.45°S, 55.45°E). *Journal of Geophysical Research: Space Physics*, *121*(4), 3198–3211. https://doi.org/10.1002/2016JA022418

Berkey, F. T., Driatskiy, V. M., Henriksen, K., Hultqvist, B., Jelly, D. H., Shchuka, T. I., et al. (1974). A synoptic investigation of particle precipitation dynamics for 60 substorms in IQSY (1964-1965) and IASY (1969). *Planetary and Space Science*, *22*(2), 255–307. https://doi.org/10.1016/0032-0633(74)90028-2

Birn, J., Thomsen, M. F., Borovsky, J. E., Reeves, G. D., McComas, D. J., & Belian, R. D. (1997). Characteristic plasma properties during dispersionless substorm injections at geosynchronous orbit. *Journal of Geophysical Research*, *102*(A2), 2309–2324. https://doi.org/10.1029/96JA02870

Boyle, C. B., Reiff, P. H., & Hairston, M. R. (1997). Empirical polar cap potentials. *Journal of Geophysical Research*, *102*(A2), 115–125. https://doi.org/10.1029/96JA01742

Chisham, G. (1996). Giant pulsations (Pgs): An explanation for their rarity and occurrence during geomagnetically quiet times. *Journal of Geophysical Research*, *101*(A11), 24755–24763. https://doi.org/10.1029/96ja02540

Clauer, C. R., & McPherron, R. L. (1974). Mapping the local time-universal time development of magnetospheric substorms using mid-latitude magnetic observations. *Journal of Geophysical Research*, *79*(19), 2811–2820. https://doi.org/10.1029/JA079i019p02811

Frey, H. U., & Mende, S. B. (2006). Substorm onsets as observed by IMAGE-FUV. In *Proceedings of the eighth international conference on substorms (ICS-8)* (pp. 71–75). University of Calgary.

Gjerloev, J. W. (2012). The SuperMAG data processing technique. *Journal of Geophysical Research*, *117*(A9), A09213. https://doi.org/10.1029/2012JA017683

Grandin, M., Aikio, A. T., Kozlovsky, A., Ulich, T., & Raita, T. (2017). Cosmic radio noise absorption in the high-latitude ionosphere during solar wind high-speed streams. *Journal of Geophysical Research: Space Physics*, *122*(5), 5203–5223. https://doi.org/10.1002/2017JA023923

Hargreaves, J. K. (1969). Auroral absorption of HF radio waves in the ionosphere: A review of results from the first decade of riometry. *Proceedings of the IEEE*, *57*(8), 1348–1373. https://doi.org/10.1109/proc.1969.7275

Hsu, T. S., & McPherron, R. L. (2007). A statistical study of the relation of Pi 2 and plasma flows in the tail. *Journal of Geophysical Research*, *112*(A5), A05209. https://doi.org/10.1029/2006JA011782

KavanaghLu, A. J. G., Donovan, E. F., Reeves, G. D., Honary, F., Manninen, J., & Immel, T. J. (2007). Energetic electron precipitation during sawtooth injections. *Annals of Geophysics*, *25*(5), 1199–1214. https://doi.org/10.5194/angeo-25-1199-2007

Kellerman, A. C., & Makarevich, R. A. (2011). The response of auroral absorption to substorm onset: Superposed epoch and propagation analyses. *Journal of Geophysical Research*, *116*(A5), A05312. https://doi.org/10.1029/2010JA015972

Kennel, C. F. (1969). Consequences of a magnetospheric plasma. *Reviews of Geophysics*, *7*(1–2), 379–419. https://doi.org/10.1029/RG007i001p00379

King, J. H., & Papitashvili, N. E. (2005). Solar wind spatial scales in and comparisons of hourly Wind and ACE plasma and magnetic field data. *Journal of Geophysical Research*, *110*(A2), A02104. https://doi.org/10.1029/2004JA010649

Koskinen, H. E. J., Lopez, R. E., Pellinen, R. J., Pulkkinen, T. I., Baker, D. N., & Bösinger, T. (1993). Pseudobreakup and substorm growth phase in the ionosphere and magnetosphere. *Journal of Geophysical Research*, *98*(A4), 5801–5813. https://doi.org/10.1029/92JA02482

Maynard, M. C. (1978). On large poleward-directed electric fields at sub-auroral latitudes. *Geophysical Research Letters*, *5*, 7–618. https://doi.org/10.1029/GL005i007p00617

McComas, D., Skoug, R., Delapp, D., Elliott, H., & Davis, A. (2022). ACE solar wind electron, proton, and alpha monitor (SWEPAM) plasma moments, level 2 (H2), 1 h data. [Dataset]. NASA Space Physics Data Facility. https://doi.org/10.48322/9w01-2555

Motoba, T., Takahashi, K., Gjerloev, J., Ohtani, S., & Milling, D. K. (2013). The role of compressional Pc5 pulsations in modulating precipitation of energetic electrons. *Journal of Geophysical Research: Space Physics*, *118*(12), 7728–7739. https://doi.org/10.1002/2013JA018912

Newell, P. T., & Gjerloev, J. W. (2011). Evaluation of SuperMAG auroral electrojet indices as indicators of substorms and auroral power. *Journal of Geophysical Research*, *116*(A12), A12211. https://doi.org/10.1029/2011JA016779

Nicholson, D. R. (1983). *Introduction to plasma theory*. John Wiley & Sons.

Nishimura, Y., Shinbori, A., Ono, T., Iizima, M., & Kumamoto, A. (2006). Storm-time electric field distribution in the inner magnetosphere. *Geophysical Research Letters*, *33*(22), L22102. https://doi.org/10.1029/2006GL027510

Nosé, M., Iyemori, T., Wang, L., Hitchman, A., Matzka, J., Feller, M., et al. (2012). Wp index: A new substorm index derived from high-resolution geomagnetic field data at low latitude. *Space Weather*, *10*(8). https://doi.org/10.1029/2012SW000785

Ozaki, M., Yagitani, S., Nagano, I., Yamagishi, H., & Sato, N. (2009). Estimation of enhanced electron density in the lower ionosphere using correlation between natural VLF emission intensity and CNA. *Antarctic Record*, *53*(2), 123–125.

Ozaki, M., Yagitani, S., Shiokawa, K., Tanaka, Y., Ogawa, Y., Hosokawa, K., et al. (2022). Slow contraction of flash aurora induced by an isolated chorus element ranging from lower-band to upper-band frequencies in the source region. *Geophysical Research Letters*, *49*(9), e2021GL097597. https://doi.org/10.1029/2021GL097597

Papitashvili, N. E., & King, J. H. (2020). OMNI 1-min data [Dataset]. NASA Space Physics Data Facility. https://doi.org/10.48322/45bb-8792

Ranta, H., Ranta, A., Collis, P. N., & Hargreaves, J. K. (1981). Development of the auroral absorption substorm: Studies of pre-onset phase and sharp onset using an extensive riometer network. *Planetary and Space Science*, *29*(12), 1287–1313. https://doi.org/10.1016/0032-0633(81)90095-7

Rosenberg, T. J., & Dudeney, J. R. (1986). The local time, substorm, and seasonal dependence of electron precipitation at L ≈ 4 inferred from riometer measurements. *Journal of Geophysical Research*, *91*(A11), 12032–12040. https://doi.org/10.1029/JA091iA11p12032

Shiokawa, K., Katoh, Y., Hamaguchi, Y., Yamamoto, Y., Adachi, T., Ozaki, M., et al. (2017). Ground-based instruments of the PWING project to investigate dynamics of the innermagnetosphere at subauroral latitudes as a part of the ERG-ground coordinated observation network. *Earth Planets and Space*, *69*(1), 160. https://doi.org/10.1186/s40623-017-0745-9

Shiokawa, K., Oyama, S., & Tanaka, Y. (2023b). Cosmic radio noise data measured with a ground 30 MHz broad-beam riometer at Gakona, USA [Dataset]. ISEE. https://doi.org/10.34515/DATA.GND-0013-0008-0101_v01]

Shiokawa, K., & Tanaka, Y. (2023). Cosmic radio noise data measured with a ground 30 MHz broad-beam riometer at Kapuskasing, Canada [Dataset]. ISEE. https://doi.org/10.34515/DATA.GND-0021-0008-0101_v01]

Shiokawa, K., Tanaka, Y., & Baishev, D. G. (2023e). Cosmic radio noise data measured with a ground 30 MHz broad-beam riometer at Zhigansk, Russia [Dataset]. ISEE. https://doi.org/10.34515/DATA.GND-0061-0008-0101_v01]

Shiokawa, K., Tanaka, Y., & Connors, M. (2023a). Cosmic radio noise data measured with a ground 30 MHz broad-beam riometer at Athabasca, Canada [Dataset]. ISEE. https://doi.org/10.34515/DATA.GND-0004-0008-0101_v01]

Shiokawa, K., Tanaka, Y., & Kadokura, A. (2023c). Cosmic radio noise data measured with a ground 30 MHz broad-beam riometer at Husafell, Iceland [Dataset]. ISEE. https://doi.org/10.34515/DATA.GND-0015-0008-0101_v01]

Shiokawa, K., Tanaka, Y., Nishitani, N., Oinats, A., Kurkin, V., & Aleshkov, V. (2023d). Cosmic radio noise data measured with a ground 30 MHz broad-beam riometer at Istok, Russia [Dataset]. ISEE. https://doi.org/10.34515/DATA.GND-0018-0008-0101_v01

Shiokawa, K., Yokoyama, Y., Ieda, A., Miyoshi, Y., Nomura, R., Lee, S., et al. (2014). Ground-based ELF/VLF chorus observations at subauroral latitudes—VLF-CHAIN Campaign. *Journal of Geophysical Research: Space Physics*, *119*(9), 7363–7379. https://doi.org/10.1002/2014JA020161

Shiokawa, K., Yumoto, K., Tanaka, Y., Osaki, H., Sato, M., Kato, T., et al. (1996). Auroral observations using automatic optical instruments: Relations with multiple Pi 2 magnetic pulsations. *Journal of Geomagnetism and Geoelectricity*, *48*(11), 1407–1419. https://doi.org/10.5636/jgg.48.1407

Smiddy, M., Kelley, M. C., Burke, W., Rich, F., Sagalyn, R., Shuman, B., et al. (1977). Intense poleward-directed electric fields near the ionospheric projection of the plasmapause. *Geophysical Research Letters*, *4*, 11–546. https://doi.org/10.1029/GL004i011p00543

Smith, C. W., & Ness, N. F. (2022). ACE magnetic field 16-second level 2 data [Dataset]. NASA Space Physics Data Facility. https://doi.org/10.48322/e0dc-0h53

Sotirelis, T., Korth, H., Hsieh, S.-Y., Zhang, Y., Morrison, D., & Paxton, L. (2013). Empirical relationship between electron precipitation and farultraviolet auroral emissions from DMSP observations. *Journal of Geophysical Research: Space Physics*, *118*(3), 1203–1209. https://doi.org/10.1002/jgra.50157

Spanswick, E., Donovan, E., & Baker, G. (2005). Pc5 modulation of high energy electron precipitation: Particle interaction regions and scattering efficiency. *Annals of Geophysics*, *23*(5), 1533–1542. https://doi.org/10.5194/angeo-23-1533-2005

Spanswick, E., Donovan, E., Friedel, R., & Korth, A. (2007). Ground based identification of dispersionless electron injections. *Geophysical Research Letters*, *34*(3), L03101. https://doi.org/10.1029/2006GL028329

Spiro, R. W., Heelis, R. A., & Hanson, W. B. (1979). Rapid subauroral ion drifts observed by atmosphere explorer C. *Geophysical Research Letters*, *6*, 8–660. https://doi.org/10.1029/GL006i008p00657

Takeshita, Y., Shiokawa, K., Ozaki, M., Manninen, J., Oyama, S.-I., Connors, M., et al. (2019). Longitudinal extent of magnetospheric ELF/VLF waves using multipoint PWING ground stations at subauroral latitudes. *Journal of Geophysical Research: Space Physics*, *124*(12), 9881–9892. https://doi.org/10.1029/2019JA026810

Tanaka, Y., Ishii, M., Kubota, M., Murayama, Y., Mori, H., & Lummerzheim, D. (2007). Cosmic noise absorption observed with imaging riometer in Alaska: Use of CNA to estimate energy spectra of auroral precipitating electrons. *Journal of the National Institute of Information and Communications Technology*, *54*(1/2).

Thomas, N., Kero, A., Miyoshi, Y., Shiokawa, K., Hyötylä, M., Raita, T., et al. (2022). Statistical survey of Arase satellite data sets in conjunction with the Finnish riometer network. *Journal of Geophysical Research: Space Physics*, *127*(5), e2022JA030271. https://doi.org/10.1029/2022JA030271

Turunen, E., Verronen, P. T., Seppälä, A., Rodger, C. J., Clilverd, M. A., Tamminen, J., et al. (2009). Impact of different energies of precipitating particles on Nox generation in the middle and upper atmosphere during geomagnetic storms. *Journal of Atmospheric and Solar-Terrestrial Physics*, *71*(10–11), 1176–1189. https://doi.org/10.1016/j.jastp.2008.07.005

Wilson, A., & Stoker, P. H. (2002). Imaging riometer observations on energetic electron precipitation at SANAE IV, Antarctica. *Journal of Geophysical Research*, *107*(A10), 1268. https://doi.org/10.1029/2000JA000463

Wing, S., Gkioulidou, M., Johnson, J. R., Newell, P. T., & Wang, C.-P. (2013). Auroral particle precipitation characterized by the substorm cycle. *Journal of Geophysical Research*, *118*(3), 1022–1039. https://doi.org/10.1002/jgra.50160

World Data Center for Geomagnetism, Kyoto, Nose, M., Iyemori, T., Sugiura, M., & Kamei, T. (2015). Geomagnetic Dst index [Dataset]. WDC. KUGI. https://doi.org/10.17593/14515-74000

World Data Center for Geomagnetism, Kyoto, & Nosé, M. (2016). Geomagnetic Wp index [Dataset]. WDC.KUGI. https://doi.org/10.17593/13437-46800

Yonezu, Y., Shiokawa, K., Connors, M., Ozaki, M., Manninen, J., Yamagishi, H., & Okada, M. (2017). Simultaneous observations of magnetospheric ELF/VLF emissions in Canada, Finland, and Antarctica. *Journal of Geophysical Research: Space Physics*, *122*(6), 6442–6454. https://doi.org/10.1002/2017JA024211